Environmental Science and Pollution Research (2022) 29:24309–24321
https://doi.org/10.1007/s11356-021-17713-x

RESEARCH ARTICLE

Carbon matrix of biochar from biomass modeling components facilitates electron transfer from zero-valent iron to Cr(VI)

Jian Zhang[1] · Xianni Yang[1] · Jun Shi[1] · Mingyue Zhao[1] · Weiqin Yin[1] · Xiaozhi Wang[1,2,3] · Shengsen Wang[1,2,3] · Changai Zhang[4]

Received: 13 September 2021 / Accepted: 19 November 2021 / Published online: 25 November 2021

Abstract

Biochar-harbored zero-valent iron (ZVI/BC) has been extensively used to detoxify hexavalent chromium (Cr(VI)). However, the role played by biochar in promoting electron transfer of ZVI and Cr(VI) reduction was not fully uncovered. Herein, three biomass modeling components (cellulose, hemicellulose, and lignin) and their blends were utilized to synthesize ZVI/BC via co-pyrolysis with hematite. X-ray diffraction analysis showed that hematite was successfully reduced to ZVI in nitrogen ambience. Batch sorption experiment showed that mass ratio (hematite to lignocellulosic component) of 1:20 is most optimal for reduction of Cr(VI) by ZVI/BCs. ZVI supported by BC derived from cellulose, hemicellulose, and their binary mixture demonstrated better Cr(VI) removal capacity (23.8–38.3 mg g^{-1}) owing to higher ordered and graphitic carbon structure as revealed by Raman spectrum. In addition, lower Tafel corrosion potentials and smaller electrochemical impedance arc radiuses were observed based on electrochemical analysis, suggesting their higher electrical conductivity and faster electron transfer, whereas the BCs derived from lignin and lignin-containing hybrids were not conducive to electron transfer of ZVI due to lower degree of graphitization, thus compromising Cr(VI) removal by ZVI/BC (7.7–17.7 mg g^{-1}). As per X-ray photoelectron spectroscopy analysis, reduction, complexation, and co-precipitation were the main mechanisms for Cr(VI) removal. The present study provided a scientific evidence for screening plant-derived biomass feedstock with high contents of cellulose and hemicellulose and low lignin content to fabricate ZVI/BC to achieve high Cr(VI) removal.

Keywords Biochar · Zero-valent iron · Electron transfer · Water remediation · Hexavalent chromium · Removal mechanism

Introduction

Potentially toxic element pollution in wastewater, especially chromium (Cr), has aroused much concern worldwide. Commonly, Cr exists in aqueous phase as two major oxidation valence states, i.e., the hexavalent (Cr(VI)) and trivalent Cr (Cr(III)) states (Zhou et al. 2016). Oxyanionic Cr(VI) is more poisonous and can threaten to function of ecosystem and human health. By contrast, cationic Cr(III) is an essential biological trace element to mammals and relatively friendly, immobile, and less toxic (Lyu et al. 2017). Thereby, reductive transformation of Cr(VI) to Cr(III) was considered as a common remediation strategy of wastewater treatment.

Zero-valent iron (ZVI) has exhibited outstanding reduction capability towards Cr(VI) because of its low standard redox potential (− 0.44 V) (Liu and Wang 2019). However, inevitable aggregation of magnetic ZVI nanoparticles and formation of passivation shell (i.e., iron oxides) resulted

Responsible Editor: Ioannis A. Katsoyiannis

✉ Shengsen Wang
wangss@yzu.edu.cn

✉ Changai Zhang
zca2006@sina.com

[1] College of Environmental Science and Engineering, Yangzhou University, Yangzhou 225127, People's Republic of China

[2] Joint International Research Laboratory of Agriculture and Agri-Product Safety of Ministry of Education of China, Yangzhou University, Yangzhou 225127, Jiangsu, China

[3] Jiangsu Collaborative Innovation Center for Solid Organic Waste Resource Utilization, Nanjing, China

[4] School of Environmental and Natural Resources, Zhejiang University of Science & Technology, Hangzhou 310023, China

in reduced removal capability towards contaminants (Shi et al. 2019). To avoid the aggregation of ZVI and increase its active site, some modification strategies such as coating with surfactants (Li et al. 2021), dispersing with supporters (Ruan et al. 2022), and sulfidation (Zhou et al. 2021a, 2021b, 2022) were investigated. As a supporter material, biochar (BC) with abundant pore structure was commonly used to disperse and harbor ZVI nanoparticles (Qian et al. 2017). Moreover, oxygen-containing functional groups in biochar (350–600 °C) were mainly electron donor components (Xu et al. 2019), while condensed aromatic carbon structure in biochar with increasing temperature (above 600 °C) functions as electron shuttle (Sun et al. 2017). In this regard, condensed aromatic carbon matrix as an electronic shuttle played an important role in facilitating electron transfer from ZVI (electron donor) to contaminants (electron acceptor) owing to its high electron conductivity (Mortazavian et al. 2018). Electrochemical analysis of pyrogenic carbon has shown that ordered and graphitic carbon structure was formed as a function of elevating temperature, which directly enhanced electron transfer (Sun et al. 2018). Thus, there is a reasonable relation between carbon structure of biochar and electron transfer of ZVI. Further, we hypothesized that the more ordered and graphitic carbon structure in BC could facilitate electron relocation of ZVI and thus improve its reduction efficiency to Cr(VI).

At a precise temperature, properties of BC depend on its organic precursors to a large extent (Zhou et al. 2021a, b, c). Plant-derived biomass mainly contains cellulose, hemicellulose, lignin, and inorganic minerals. Cellulose is a long-chain glucose polymer (Wu et al. 2018) and has a large proportion in biomass, while hemicellulose is a complex and heterogeneous polymeric network and mainly includes xylose (Giudicianni et al. 2013). Lignin is a polyaromatic compound that contains three phenyl propane monomers (Wu et al. 2018). Therefore, the three components could also function as biochar precursors. It was reported that cellulose and hemicellulose degraded at 375–450 and 250–300 °C, respectively (Yu et al. 2017), while lignin degraded gently in 100–800 °C range (Ma et al. 2019), resulting in different solid char production. For instance, char mass production of cellulose and hemicellulose pyrolyzed at 850 °C was ~ 17–20%, while solid composition of lignin was ~ 41% under the same condition (Ma et al. 2019).

Moreover, during practical pyrolysis of lignocellulosic biomass, synergetic or antagonistic interaction among these three components could not be ignored, as revealed by previous studies (Yu et al. 2017; Wu et al. 2018). In our previous study, Cr(VI) removal capacity was similar for the ZVI supported by BC derived from synthetic lignocellulosic blends with or without the addition of inorganic ash, and BC properties are significantly inherited from three biomass modeling compounds (Zhou et al. 2021a, b, c). Thus, inorganic minerals were not considered in the component interaction assessment in the co-pyrolysis process. Recent studies found that syngases' production decreased during the cellulose-lignin co-pyrolysis process (Wu et al. 2018). Therefore, interaction among cellulose, hemicellulose, and lignin during pyrolysis could also affect physicochemical property and electron transfer capacity of biochar. Further, if cellulose, hemicellulose, lignin, and their blends were used as biochar precursors to harbor ZVI, reduction capability of prepared composites toward Cr(VI) would be also different. However, few and limited studies were performed to investigate the impact of pyrogenic carbon matrix of biochar from the three components and their blends on elimination of Cr(VI) onto ZVI/BC.

In addition, high-temperature thermal reduction is an effective method for synthesis of ZVI/BC because biochar can be as a protective layer for ZVI compared to conventional aqueous phase reduction of Fe^{2+} or Fe^{3+} by borohydride. Our previous study confirmed successful phase transformation of hematite to Fe^0 through co-pyrolysis pinewood biomass and natural hematite (Wang et al. 2019b). In the present study, 800 °C was selected as the preparation temperature of ZVI/BC based on a consideration that hematite can be transformed to ZVI to a higher degree, and that the lignocellulosic components were carbonized with a different extent to obtain different conductivity (Fan et al. 2020; Zhao et al. 2020). More importantly, catalytic capability of iron oxide and its phase transformation were confirmed through co-pyrolysis of iron oxide and cellulose mixture (Hoekstra et al. 2016). Amorphous carbon was transferred to graphitic carbon, concurrently iron oxide was reduced to metallic Fe, forming the iron-induced carbon-encapsulated iron nanoparticles with core–shell structure, namely, Fe^0 and Fe_3C as a core and graphitic carbon layer as a shell (Hoekstra et al. 2016; Neeli and Ramsurn 2018), which can be conducive to the electron transfer of ZVI to Cr(VI). However, the role of this quasi core–shell structure in enhancing electronic transfer from ZVI to Cr(VI) was understood poorly.

Hence, the present study aimed to (i) fabricate and characterize ZVI/BC via co-pyrolysis of hematite and cellulose, hemicellulose, lignin, and their blends, (ii) estimate the removal capacity of Cr(VI) by as-prepared ZVI/BC, and (iii) uncover the roles of BC from biomass modeling components in facilitating Cr(VI) removal by ZVI/BC.

Materials and methods

Chemical reactants

Xylan was used to represent hemicellulose and bought from Macklin Chemical Reagent Co., Ltd. Microcrystalline

cellulose, dealkalined lignin, hematite (Fe_2O_3), potassium dichromate ($K_2Cr_2O_7$), hydrochloric acid (HCl), sodium hydroxide (NaOH), potassium chloride (KCl), monopotassium phosphate (KH_2PO_4), nitric acid (HNO_3), acetone, sulfuric acid (H_2SO_4), phosphoric acid (H_3PO_4), 1,5-diphenylcarbohydrazide, and potassium ferricyanide [$K_3Fe(CN)_6$] were from Sinopharm Chemical Reagent Co., Ltd. Deionized (DI) water (18.2 MΩ) was used to prepare solutions.

Preparation of biochar and biochar-harbored ZVI composites

For biochar preparation, 2.0 g of cellulose, hemicellulose, and lignin was pyrolyzed at 800 °C under N_2 atmosphere according to a previous study (Zhao et al. 2020) and the obtained biochar was named as BC_{CE}, BC_{HE}, and BC_{LG}, respectively. For biochar-supported ZVI composites synthesis, the suitable mass ratio of single component and hematite was firstly investigated via taking microcrystalline cellulose as an example. The hematite to cellulose mass ratio was considered at 1:5, 1:10, 1:20, and 1:40. The mixture was stirred mechanically for well dispersion and then was pyrolyzed at 800 °C for 2 h in N_2 atmosphere (Zhao et al. 2020). The obtained composites was named as ZVI/$BC_{CE(1:5)}$, ZVI/$BC_{CE(1:10)}$, ZVI/$BC_{CE(1:20)}$, and ZVI/$BC_{CE(1:40)}$. Samples were washed using DI water and ethanol for three times and then dried at 60 °C for 24 h under oxygen-free condition.

Cellulose, hemicellulose, and lignin were mixed with hematite at a biomass to hematite ratio of 20:1, respectively, based on the Cr(VI) removal capacity obtained above. The three mixtures were co-pyrolyzed as above, and resulting samples were named as ZVI/BC_{CE}, ZVI/BC_{HE}, and ZVI/BC_{LG}. Cellulose, hemicellulose, and lignin were mixed in the same mass proportion and in binary or ternary forms, i.e., cellulose + hemicellulose (CH), cellulose + lignin (CL), hemicellulose + lignin (HL), and cellulose + hemicellulose + lignin (CHL). The four blends were co-pyrolyzed as above, and resulting samples were denoted as ZVI/BC_{CH}, ZVI/BC_{CL}, ZVI/BC_{HL}, and ZVI/BC_{CHL}.

Batch sorption experiment

In adsorption experiment, pH of Cr(VI) solution was regulated to 3.0 ± 0.1 with 0.1 M HCl and 0.1 M NaOH (Zhou et al. 2021a, b, c). Added into 25-mL centrifuge tubes with Cr(VI) solution (10 mL and 50 mg L^{-1}) was 0.01 g of sorbents (1 g L^{-1}). The suspension was vibrated on a rotary shaker at 25 ± 0.5 °C and sampled at 24 h. Then, the suspension was immediately filtered using 0.22-μm membrane. Cr(VI) concentration in the filtrates was measured using the diphenyl carbohydrazide colorimetric method (Zhao et al. 2020). The concentration of total Cr was determined by an ICP-AES. The concentration of Cr(III) was obtained using the minus method. The adsorption capacity calculation formula is listed in text S1 of supplementary information.

Electrochemical experiment

The electrochemical method was used to characterize the electron transfer and electrical conductance properties of BC and ZVI/BC composites (Mortazavian et al. 2018; Xu et al. 2019). In the present study, electrochemical experiment was finished at an electrochemical workstation (CHI760E, Beijing Chinese science days Technology Co., Ltd), which includes three electrodes (i.e., working electrode, reference electrode, and platinum counter electrode).

The electrochemical impedance spectroscopy can characterize electrical conductance of BC and ZVI/BC composites (Dong et al. 2018), which was determined in 0.1 M KCl and 5.0 mM $K_3Fe(CN)_6$ solution. Tafel corrosion curves can describe the electron transfer rate (Mortazavian et al. 2018), which were obtained in Cr(VI) solutions (50 mg L^{-1}) with purification using argon gas.

Characterization of composites

The elemental contents in sorbents were measured using an element analyzer. Specific surface area, pore size, and pore volumes were analyzed with an ASAP2460 analyzer and calculated according to Brunauer–Emmett–Teller (BET) and Barrett-Joyner-Halenda (BJH) methods. The morphologies of BC and ZVI/BC composites were characterized using a scanning electron microscope (SEM) (S-4800II Scanning Microscope) and a transmission electron microscopy (TEM). Raman spectra was used to analyze carbon structure of sorbents. X-ray diffractometer (XRD) was utilized to identify Fe-bearing crystals phase in sorbents. Thermogravimetric analyses (TGA) (Perkin-Elmer Pyris 1, USA) was used to analyze the thermal stability of three components. Differential thermogravimetric (DTG) curve was used to present mass loss rate based on the first derivative of TGA data. The valence states of oxygen, C, Fe, and Cr were measured using an X-ray photoelectron spectroscopy (XPS).

Results and discussion

TGA, BET surface area, and morphology

Physicochemical characteristics of three BCs and ZVI/BCs composites are listed in Table 1. Compared to BC_{LG}, greater C content were observed for BC_{CE} and BC_{HE}, with an inverse trend of N content, which was similar to our previous study (Zhou et al. 2021a, b, c). The char yields of BC_{CE} (11.5%), BC_{HE} (16%), and BC_{LG} (40.7%) indicated different thermal stability of cellulose, hemicellulose, and

Table 1 Physicochemical properties of biochars (BCs) from cellulose (BC_{CE}), hemicellulose (BC_{HE}), and lignin (BC_{LG}) and zero-valent iron (ZVI) supported by them

Biochar and ZVI/BC	N (%)	H (%)	C (%)	Char yield (%)	BET surface area ($m^2\ g^{-1}$)	Porous size (nm)	Porous volume ($cm^3\ g^{-1}$)
BC_{CE}	0.17	2.03	87.57	11.5	432.95	1.94	0.21
BC_{HE}	0.10	1.98	85.40	16	279.84	1.93	0.135
BC_{LG}	0.30	1.72	74.52	40.7	1.45	4.20	0.0015
ZVI/BC_{CE}	0.14	0.99	67.01	-	259.98	2.70	0.175
ZVI/BC_{HE}	0.09	0.69	80.46	-	257.53	3.21	0.207
ZVI/BC_{LG}	0.24	1.39	63.85	-	5.96	4.87	0.0073

Char yield = $M_1/M_2 \times 100\%$; M_1 means the mass of the obtained biochar, and M_2 is the mass of initial biomass modeling components

lignin until 800 °C, as demonstrated by TGA and DTG analyses (Fig. 1). A similar study indicated that char yields of cellulose, hemicellulose, and lignin were 17, 20, and 41%, respectively at 850 °C (Ma et al. 2019). The thermal decomposition curves (Fig. 1) showed that cellulose exhibited sharp mass loss under a narrow temperature range of 325–375 °C. This can be ascribed to its crystalline structure and chemical stability (Dhyani and Bhaskar 2018). Hemicellulose degradation quickly decomposed from 225 to 325 °C. The reason is that hemicellulose is composed of various saccharides with amorphous structure and less stability (Ma et al. 2019). In comparison, the decomposition of lignin was slow from ambient temperature to 800 °C, ascribing to its highly cross-linked network structure with phenylpropane units (Ma et al. 2018).

Moreover, the BET specific surface area of BC_{LG} was obviously lower than those of BC_{CE} and BC_{HE}, resulting from the easier depolymerization of cellulose and hemicellulose and the stronger pore-forming effect. However, the specific surface area of ZVI/BC_{CE} significantly reduced, indicating that ZVI particles were mainly distributed in the pores of BC_{CE}. However, the surface area of ZVI/BC_{HE} reduced with a small degree. For ZVI/BC_{LG}, ZVI promoted the generation of pores in BC_{LG} and increases the specific surface area of composite. Therefore, BC_{CE} can be more suitable for supporting and dispersing ZVI particles. The N_2 adsorption–desorption isotherms of ZVI/BC_{CE}, ZVI/BC_{HE}, and ZVI/BC_{LG} and their pore width distribution diagram are displayed in Fig. 2, and the corresponding textural parameters are summarized in Table 1. According to the classification of International Union of Pure and Applied Chemistry (IUPAC), the adsorption–desorption isotherms sharp of ZVI/BC_{CE} and ZVI/BC_{HE} were observed to be type IV curves with H2 hysteresis loops at $P/P_0 = 0.45–0.95$, ascribing to the characteristic of mesoporous structure (Fig. 2a). The pore size distribution pattern of ZVI/BC_{CE} and ZVI/BC_{HE} demonstrated the centered peaks at 3.64 and 3.94 nm (Fig. 2b), and the averaged pore size was calculated as 2.70 and 3.21 nm, respectively (Table 1), indicating the typical mesoporous features. However, the N_2 adsorption–desorption isotherm of ZVI/BC_{LG} indicated an extremely low adsorption capacity, demonstrating the extremely weak porosity.

Morphological characteristics of three BCs and ZVI/BCs composites are shown in Fig. 3. BC_{CE} was a short fibrous structure (Fig. 3a), and BC_{HE} was agglomerated fibrous structure after high temperature pyrolysis (Fig. 3b). By contrary, BC_{LG} was irregular, spherical, and aggregated structure (Fig. 3c). In terms of the prepared composites, ZVI/BC_{CE} and ZVI/BC_{HE} were lamellar structure with more pores, whereas ZVI/BC_{LG} was irregularly agglomerated and spherical with relatively less pores (Fig. 3d, e, and f). Moreover, the further TEM images of ZVI/BC_{CE} and ZVI/BC_{HE} showed quasi core–shell structure with ZVI cores surrounded by film-like gray carbon shells (Fig. 3g and h). This phenomenon was ascribed to the interaction of ZVI and C at high temperatures, and the C shell could prevent ZVI from massive passivation and simultaneously enhance electron transfer of ZVI (Neeli and Ramsurn 2018). Regarding ZVI/BC_{LG}, an intensive agglomeration of ZVI was clearly observed in its TEM image (Fig. 3i).

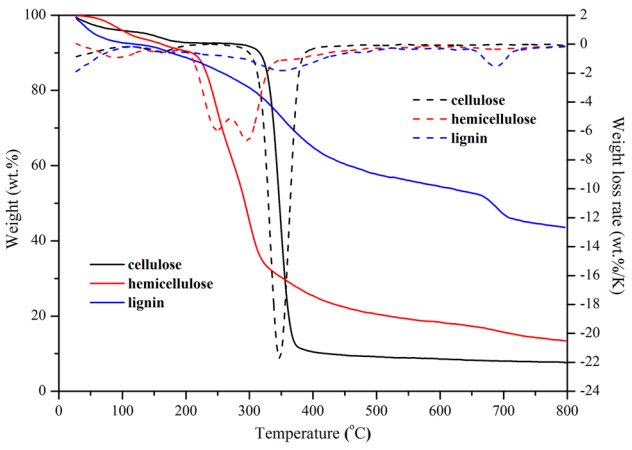

Fig. 1 Thermogravimetric analytical (TGA) and differential thermogravimetric (DTG) curves of decomposition of cellulose, hemicellulose, and lignin

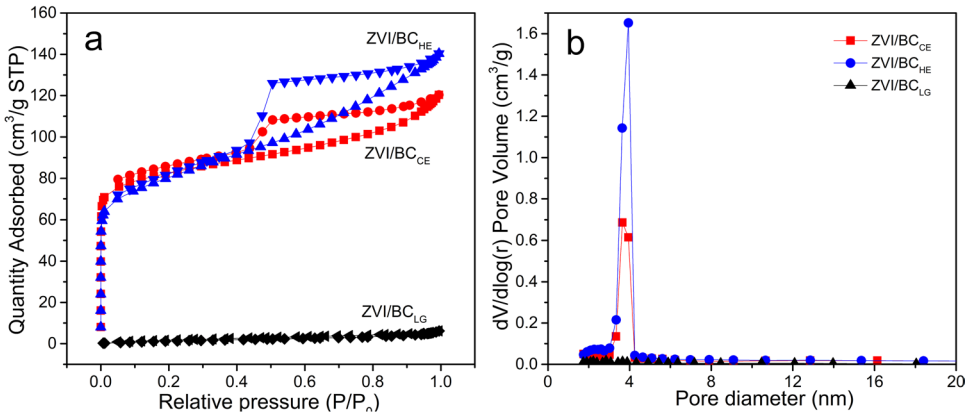

Fig. 2 N_2 adsorption–desorption isotherms of ZVI/BC_{CE}, ZVI/BC_{HE}, and ZVI/BC_{LG} (**a**) and their pore width distribution diagram (**b**)

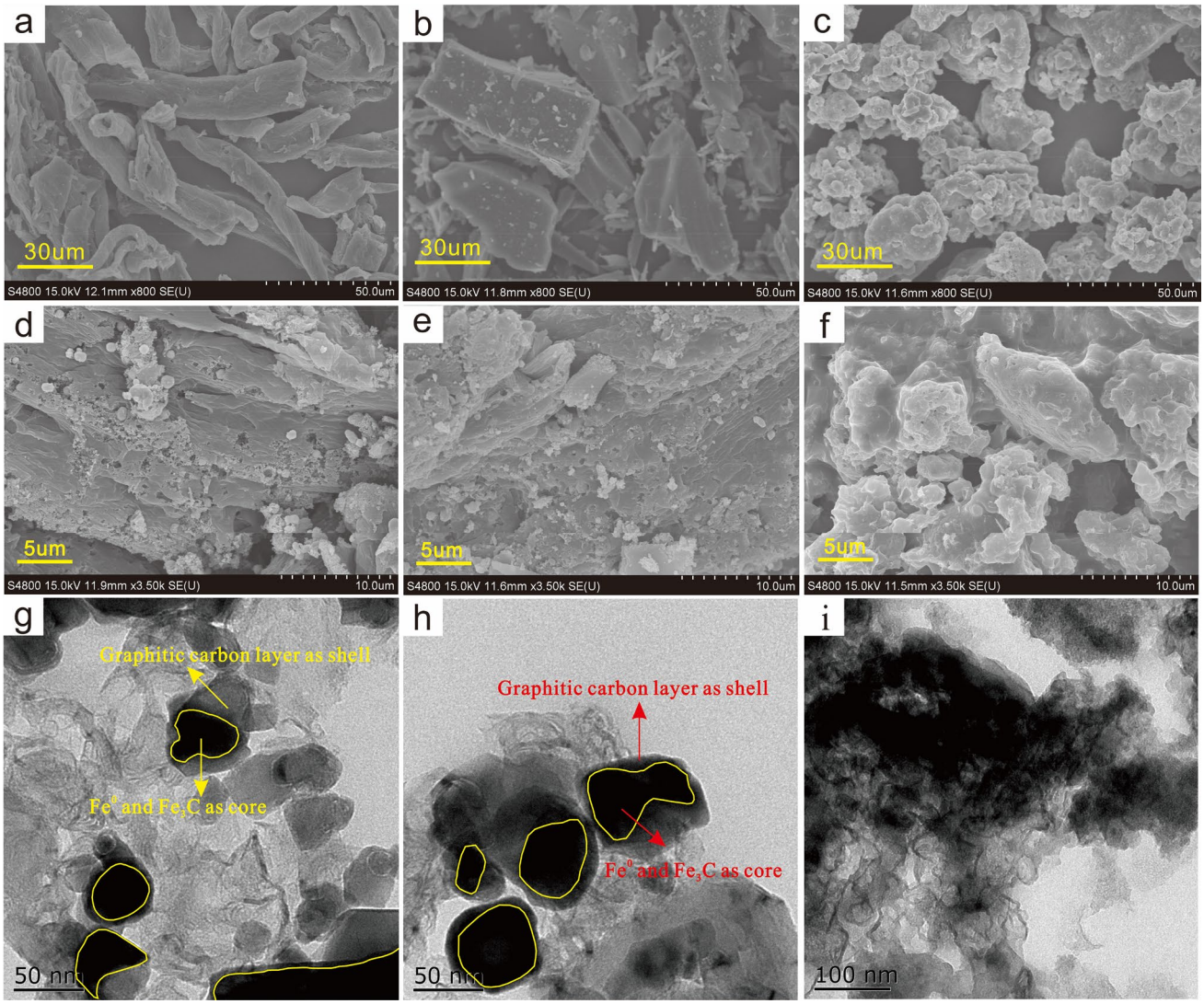

Fig. 3 Scanning electron microscope (SEM) images of biochar (BC) and BC-supported zero-valent iron (ZVI/BC) including cellulose (BC_{CE}) (**a**), hemicellulose (BC_{HE}) (**b**), lignin (BC_{LG}) (**c**), ZVI/BC_{CE} (**d**), ZVI/BC_{HE} (**e**), and ZVI/BC_{LG} (**f**). Transmission electron microscopy (TEM) images of ZVI/BC_{CE} (**g**), ZVI/BC_{HE} (**h**), and ZVI/BC_{LG} (**i**)

XRD and Raman spectra

The XRD diffraction patterns and Raman spectra of ZVI/BC_{CE} derived from different mass ratio of hematite to cellulose are shown in Fig. 4. ZVI characteristic peaks with high intensity (2θ = 44.5° and 65.1°) in the XRD pattern (Fig. 4a) showed that hematite was successfully reduced to ZVI during the pyrolysis process. The thermal transformation of hematite to ZVI can be achieved under CO at 750–900 °C (Monazam et al. 2014) and 5% H_2 + 95% N_2 atmosphere at 700–800 °C (Chen, 2017). Herein, thermal reduction of hematite under N_2 atmosphere was effective because of reductive syngas generation from decomposition of biomass, in which hematite underwent phase transformation of α-Fe_2O_3-FeO-ZVI, in line with our recent study (Zhao et al. 2020).

Furthermore, the degree of crystallinity and crystalline size of ZVI/BC_{CE} from different mass ratio were calculated according to the following equations.

$$\text{Crystallinity} = \frac{Totalareaofcrystallinepeaks}{Totalareaofallpeaks(crystalline + amorphous)} \times 100\%$$

$$\text{D (nm)} = \frac{K\lambda}{\beta\cos\theta}$$

Here, D is crystalline size, which is calculated according to the Scherrer's formula, including Scherrer's shape constant (K = 0.9), the wavelength of X-ray (λ), the full width at the half maximum of the considered peak (FWHM), namely, β, and Bragg's angle (θ) (Zhou et al. 2021b, 2022). Compared to hematite and cellulose ratio between 1:5 and 1:20, the composite ZVI/$BC_{CE(1:40)}$ owned lower degree of crystallinity (20.73%) and the smaller crystal size (30.8 nm) (Fig. S1), which was related to the lower iron loaded ratio and better dispersion. Meanwhile, distinct from the graphitic C peak at 2θ = 26.4° in ZVI/$BC_{CE(1:5)}$, ZVI/$BC_{CE(1:10)}$, and ZVI/$BC_{CE(1:20)}$ (Wang et al. 2019c), there appeared an amorphous and disordered carbon peak at 2θ = 24.8° in ZVI/$BC_{CE(1:40)}$ presenting coke carbonaceous phase (Neeli and Ramsurn 2018). It was reported that iron can catalyze carbonization of biomass and induce formation of graphite carbon (Neeli and Ramsurn 2018). Thus, the amorphous and disordered carbon in ZVI/$BC_{CE(1:40)}$ can be resulted from low iron availability for C catalysis. By contrast, in addition to ZVI peaks, extra peaks 2θ = 41.2°, 43.3°, 43.8°, and 47.9° corresponding to Fe_3C phase were clearly observed (Jiang et al. 2019b; Mian and Liu 2019; Wang et al. 2019c), further implying that Fe^0 could react with C. Raman spectra of ZVI/BC_{CE} derived from different mass ratio showed that the D and G band peak intensity ratio (I_D/I_G) of ZVI/$BC_{CE(1:20)}$ reached the highest, demonstrating the greatest graphitization of ZVI/$BC_{CE(1:20)}$ (Sun et al. 2017; Yu et al. 2020) (Fig. 4b). The D peak in Raman spectral mapping corresponding to the ring breathing vibration mode of carbon usually refers to the signal of the disorder in graphitic carbon structure, and the G peak generally corresponds to the in-plane vibration mode of sp^2-hybridized carbon (graphite carbon) (Sun et al. 2017). The higher I_D/I_G value, the more number and clusters of aromatic rings (Yu et al. 2020). Therefore, the mass ratio of 1: 20 was chosen to analyze effects of different biomass modeling compounds on characteristics of ZVI/BC composites.

The XRD patterns (Fig. S2a) of ZVI/BC_{CE}, ZVI/BC_{HE}, and ZVI/BC_{LG} showed obvious ZVI peak (2θ = 44.8° and 65.1°), whereas ZVI peak intensity in ZVI/BC_{LG} was lower than ZVI/BC_{CE} and ZVI/BC_{HE}, possibly resulting from the lower syngas formation of lignin depolymerization until 800 °C. Additionally, the amorphous C peak at 2θ = 24.8°

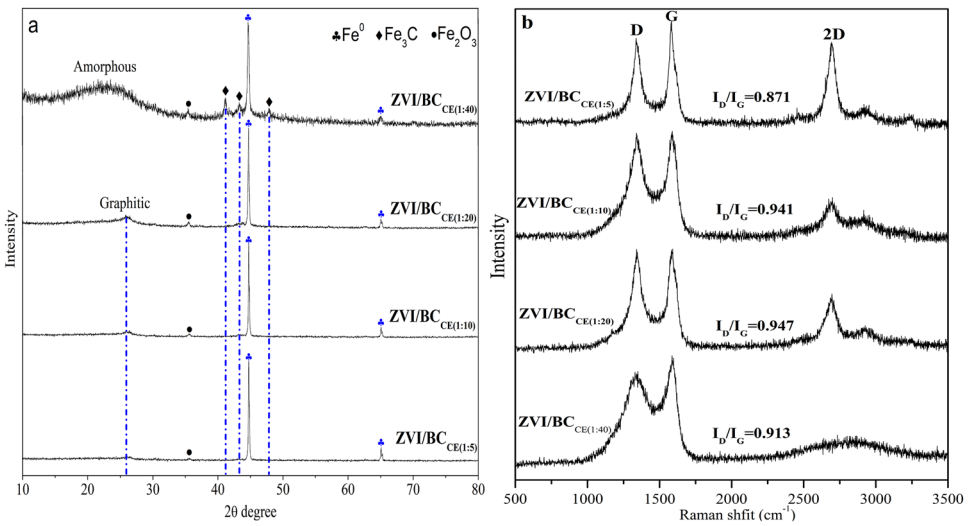

Fig. 4 XRD diffraction patterns (**a**) and Raman spectra (**b**) for ZVI/BC_{CE} prepared from different mass ratios of hematite to cellulose including 1:5, 1:10, 1:20, and 1:40

in ZVI/BC_{LG} and graphitic C peak at 2θ = 26.4° in ZVI/BC_{CE} and ZVI/BC_{HE} revealed low graphitization of lignin and amorphous nature of lignin-derived BC (Gindl-Altmutter et al. 2019; Jiang et al. 2019a). Raman pattern (Fig. S2b and S2c) exhibited BC_{LG} and ZVI/BC_{LG} had the lowest I_D/I_G value. After hematite was catalyzed, ZVI/BC_{LG} still had the lowest I_D/I_G ratio and almost no 2D peak, which was related to its amorphous carbon structure. Additionally, the I_D/I_G ratio and evident 2D peak intensity of ZVI/BC_{CE} were higher than those of ZVI/BC_{HE} and ZVI/BC_{LG}, indicating its more graphitic structure (Ye et al. 2019).

In terms of ZVI/BCs from the blended biomass modeling compounds, their characteristic peaks of ZVI (44.8° and 65.1°) showed the successful synthesis of ZVI (Fig. 5a). In addition, the peak around 2θ = 26.4° revealed that the graphitic carbon structure existed in ZVI/BC_{CH} (Johra et al. 2014). The peak around 2θ = 24.8° revealed that amorphous and disordered carbon existed in ZVI/BC_{CL} (Xu et al. 2005). The I_D/I_G ratio of ZVI/BC_{CH} was the highest (0.972) in the four composites (Fig. 5b), showing its greater degree of graphitization, which is consistent with the XRD analysis result (Fig. 5a) (Jiang et al. 2019b). Additionally, the evident 2D-band peak of ZVI/BC_{CH} indicated its better hexagonal symmetry in the structure of carbons through the formation of the graphite structure (Wang et al. 2013; Zhang et al. 2018b; Ye et al. 2019). It was demonstrated that carbonization and graphitization significantly influence on electrical conductivity of biochar via a likely mechanism of electron hopping (Gabhi et al. 2020). Thus, ZVI/BC_{CH} can exhibit better electrical conductivity than ZVI/BC_{CHL}, ZVI/BC_{CL}, and ZVI/BC_{HL}.

Cr(VI) removal by ZVI/BC_{CE} from different mass ratio

Cr(VI) removal result by ZVI/BC_{CE} prepared by different mass ratio of hematite and cellulose is indicated in Fig. 6. When the initial hematite to cellulose mass ratio

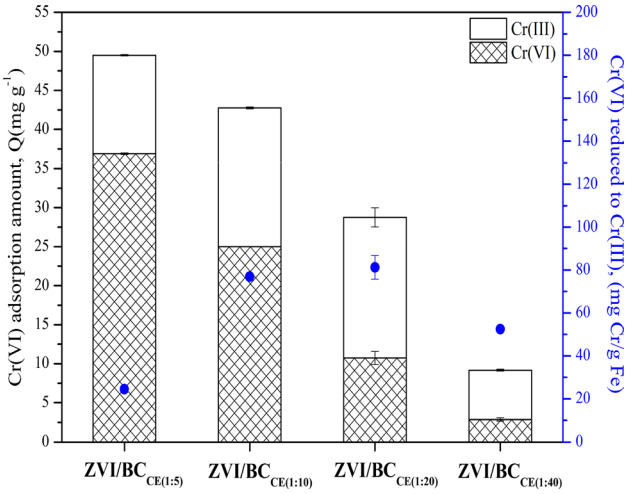

Fig. 6 Adsorption and reduction of Cr(VI) by ZVI/BC_{CE} at mass ratio of 1:5, 1:10, 1:20, and 1:40 (hematite:cellulose) (condition: Cr(VI) concentration, 50 mg L^{-1}; pH value, 3.0 ± 0.1; temperature, 20 ± 0.5 °C; reaction time, 24 h)

enhanced from 1:40 to 1:5, removal capacity for Cr(VI) was improved from 9.18 to 49.51 mg g^{-1}, showing ZVI served as the major sites in terms of Cr(VI) removal. In this regard, although the crystal size of ZVI/$BC_{CE(1:40)}$ is the lowest (30.81 nm), its removal capacity to Cr(VI) was also the lowest, ascribing to the lowest Fe loaded amount. Moreover, ZVI/BC_{CE} from different mass ratio showed the different degree of crystallinity and ZVI/$BC_{CE(1:5)}$ possessed the greatest crystallinity (71.16%), probably revealing that higher crystallinity can improve the removal performance of the materials (Zhao et al. 2022) (Fig. S1). It was affirmed that reduction of Cr(VI) is an important detoxification mechanism by ZVI and ZVI/BC (Wang et al. 2019a). To obtain the overall reductive capacity of as-prepared sorbents, the Cr(III), both in post-reaction

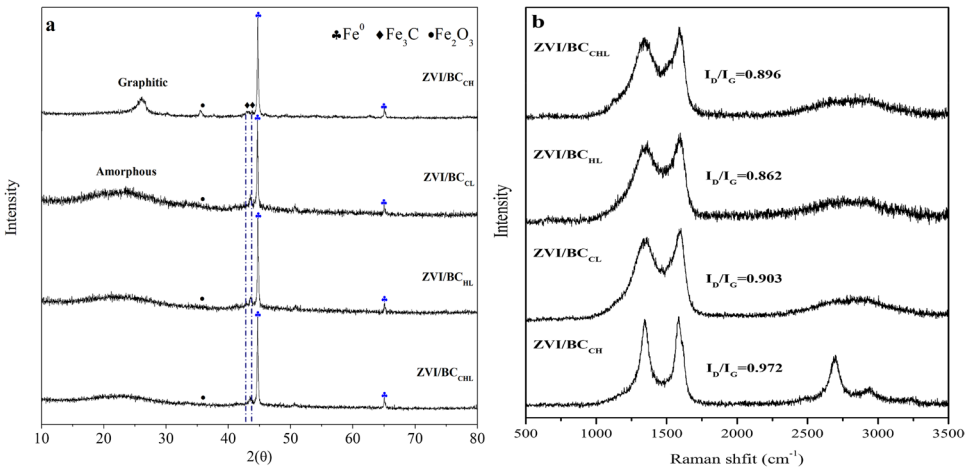

Fig. 5 XRD diffraction patterns (**a**) and Raman spectra (**b**) for ZVI/BC_{CH}, ZVI/BC_{CL}, ZVI/BC_{HL}, and ZVI/BC_{CHL}

solution as Cr(III) ion and on sorbents retained via surface complexation or precipitation, were then quantified.

Although ZVI/$BC_{CE(1:5)}$ has a higher iron loading (Table S1), its reductive capability of Cr(VI) to Cr(III) was relatively low (~ 12.61 mg g^{-1}). This indicated that a suitable iron loading amount could enhance Cr(VI) reduction. Excessive ZVI particles on biochar surface can aggregate, occupy, and reduce reactive active sites, thus resulting in decrease of Cr(VI) reduction (Dong et al. 2017; Zhu et al. 2018). In comparison, ZVI/$BC_{CE(1:10)}$ (18.02 mg g^{-1}) and ZVI/$BC_{CE(1:20)}$ (17.76 mg g^{-1}) exhibited better Cr(VI) reduction capacity than ZVI/$BC_{CE(1:5)}$ and ZVI/$BC_{CE(1:40)}$. Furthermore, the reduction of Cr(VI) by ZVI/$BC_{CE(1:20)}$ on unit mass Fe basis was 80.08 mg Cr/g Fe, which was higher than that of ZVI/$BC_{CE(1:10)}$ (78.32 mg Cr/g Fe), indicating more efficient electron transfer and better reduction performance of ZVI/$BC_{CE(1:20)}$. This is supported by the highest ratio of the D band to G band peak intensity (Fig. 4b) and the greatest degree of graphitization (Fig. 4a) of ZVI/$BC_{CE(1:20)}$. Therefore, the mass ratio of 1: 20 (hematite:biomass) was chosen as an optimal ratio for subsequent experiments.

Effect of lignocellulosic components on Cr(VI) removal

Cr(VI) removal capacities by ZVI/BC_{CE}, ZVI/BC_{HE}, and ZVI/BC_{LG} were 30.83, 23.77, and 17.68 mg g^{-1}, in which reduction made a proportion of 55.14%, 51.45%, and 46.50% of overall Cr(VI) removal, respectively (Fig. 7a). This suggested that BC_{CE} is more conducive to electron transfer of ZVI than BC_{HE} and BC_{LG}, which is possibly ascribed to graphitic carbon structures as inferred by the highest ratio of D to G peak intensity (Fig. S1c) (Lin et al. 2020).

In terms of binary and ternary components, total Cr(VI) removal capacity (Fig. 7b) by ZVI/BC_{CH} was 38.29 mg g^{-1}, which was higher than 30.83 and 23.77 mg g^{-1} of single ZVI/BC_{CE} and ZVI/BC_{HE}, respectively. The results were in accordance with our previous study (Zhou et al. 2021a, b, c), demonstrating that there was a synergistic interaction between cellulose and hemicellulose during pyrolysis which facilitated Cr(VI) removal (Wu et al. 2016). The lower Cr(VI) removal capacities were observed for of ZVI/BC_{CHL}, ZVI/BC_{CL}, and ZVI/BC_{HL}, which were 13.54, 11.70, and 7.72 mg g^{-1}, respectively. Cr(VI) reduction by different sorbents demonstrated similar trends as overall Cr(VI) removal. Raman and XRD results confirmed that pyrolysis of blends of cellulose and hemicellulose resulted in a BC with more ordered and graphitic carbon structure, enhancing electron conductivity and electron transfer of ZVI/BC_{CH} (Fig. 5b). By contrast, compromised Cr(VI) reduction by ZVI/BC_{CHL}, ZVI/BC_{CL}, and ZVI/BC_{HL} resulted from amorphous C structure and low graphitization degree of carbon from lignin (Zhou et al. 2021a, b, c). Moreover, Cr(VI) removal performance by some reported ZVI/BC composites was compared with the present removal capacity, which was displayed in Table S2. The adsorption capacity of ZVI/BC_{CH} was 38.29 mg g^{-1}, which were higher than those of other adsorbents, indicating the excellent performance. Since the essence of reduction of Cr(VI) is electron transfer from ZVI, as an electron donor, to Cr(VI) as an electron acceptor, we hypothesized that electrochemical properties of ZVI/BC composites can be further used to explain the reduction capacity of ZVI/BC composites toward Cr(VI).

Electrochemical analysis

Tafel corrosion curves and electrochemical impedance spectroscopy (EIS) Nyquist plots of ZVI/BC_{CE} prepared from different mass ratio of hematite to cellulose is shown in Fig. S3. The corrosive potential of Tafel corrosion curve of these composites indicated a trend of ZVI/$BC_{CE(1:10)}$ < ZVI/$BC_{CE(1:20)}$ < ZVI/$BC_{CE(1:5)}$ < ZVI/$BC_{CE(1:40)}$ (Fig. S3a), revealing the faster electron transfer rate of ZVI/$BC_{CE(1:10)}$ and ZVI/$BC_{CE(1:20)}$. The lower the corrosive potential of Tafel corrosion curve is, the faster the electron transfer rate of materials (Mortazavian et al. 2018). In addition, it was reported that the electrical conductivity of composites can be characterized using the EIS Nyquist curves, in which the radius of the semicircle characterizes the electron transfer resistance, namely, a smaller radius indicated a strong ability of electron transfer (Zhang et al. 2018a). According to our previous study, electrical resistance of ZVI/BC (1000 °C)

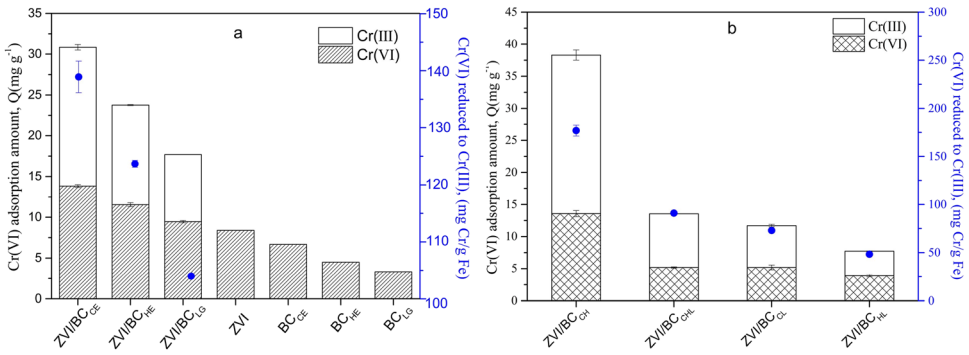

Fig. 7 Adsorption and reduction of Cr(VI) by ZVI/BC_{CE}, ZVI/BC_{HE}, and ZVI/BC_{LG} (**a**) and ZVI/BC_{CH}, ZVI/BC_{CL}, ZVI/BC_{CHL}, and ZVI/BC_{HL} (**b**) (condition: Cr(VI) concentration, 50 mg L^{-1}; pH value, 3.0 ± 0.1; temperature, 20 ± 0.5 °C; reaction time, 24 h). The removal capacity of ZVI was cited from our previous study (Zhao et al. 2020)

and ZVI was 53 and 60 Ω, respectively, indicating that the electron transfer resistance of ZVI/BC was lower, which was more conducive to electron transfer than alone ZVI (Zhao et al. 2020). The EIS Nyquist plots of $ZVI/BC_{CE(1:10)}$ and $ZVI/BC_{CE(1:20)}$ display smaller arc radiuses than those of $ZVI/BC_{CE(1:5)}$ and $ZVI/BC_{CE(1:40)}$ (Fig. S3b), indicating that the two ratios (i.e., 1:10 and 1:20) have lower electron transfer resistance and higher electric conductivity (Guo et al. 2020), which agrees with the results of Tafel corrosion curve.

Moreover, the corrosive potential of Tafel corrosion curve indicated a trend of $ZVI/BC_{CE} < ZVI/BC_{HE} < ZVI/BC_{LG}$ for biochar from single biomass model component (Fig. 8a) and $ZVI/BC_{CH} < ZVI/BC_{CHL} < ZVI/BC_{CL} < ZVI/BC_{HL}$ for mixed components (Fig. 8c). This result indicated that ZVI/BC_{CE} and ZVI/BC_{CH} possessed faster electron transfer rates in the presence of Cr(VI) (Zhao et al. 2020; Zhou et al. 2021a, b, c). In this regard, the quasi core–shell structure of ZVI/BC_{CE} and ZVI/BC_{HE} played an important role in improving the process of electron transfer. The conductive graphitic external layer facilitates the electron transfer from zero-valent iron to Cr(VI). In addition, according to Fig. 8b and d, ZVI/BC_{CE} and ZVI/BC_{CH} showed smaller impedance arc radiuses than those of ZVI/BC_{HE} and ZVI/BC_{LG} for composites from single component pyrolysis and ZVI/BC_{CHL}, ZVI/BC_{CL}, and ZVI/BC_{HL} for mixed components co-pyrolysis, suggesting the enhanced electronic conductivity and alleviative electron-transfer resistance for ZVI/BC_{CE} and ZVI/BC_{CH} (Zhang et al. 2018a). This EIS Nyquist result was consistent with the corrosive potential variation tendency of Tafel corrosion curve of composites. Therefore, greater electronic conductivity of ZVI/BC_{CE} and ZVI/BC_{CH} resulted from the high degree of graphitization and carbonization of carbon matrix in composite facilitated reduction and removal of Cr(VI).

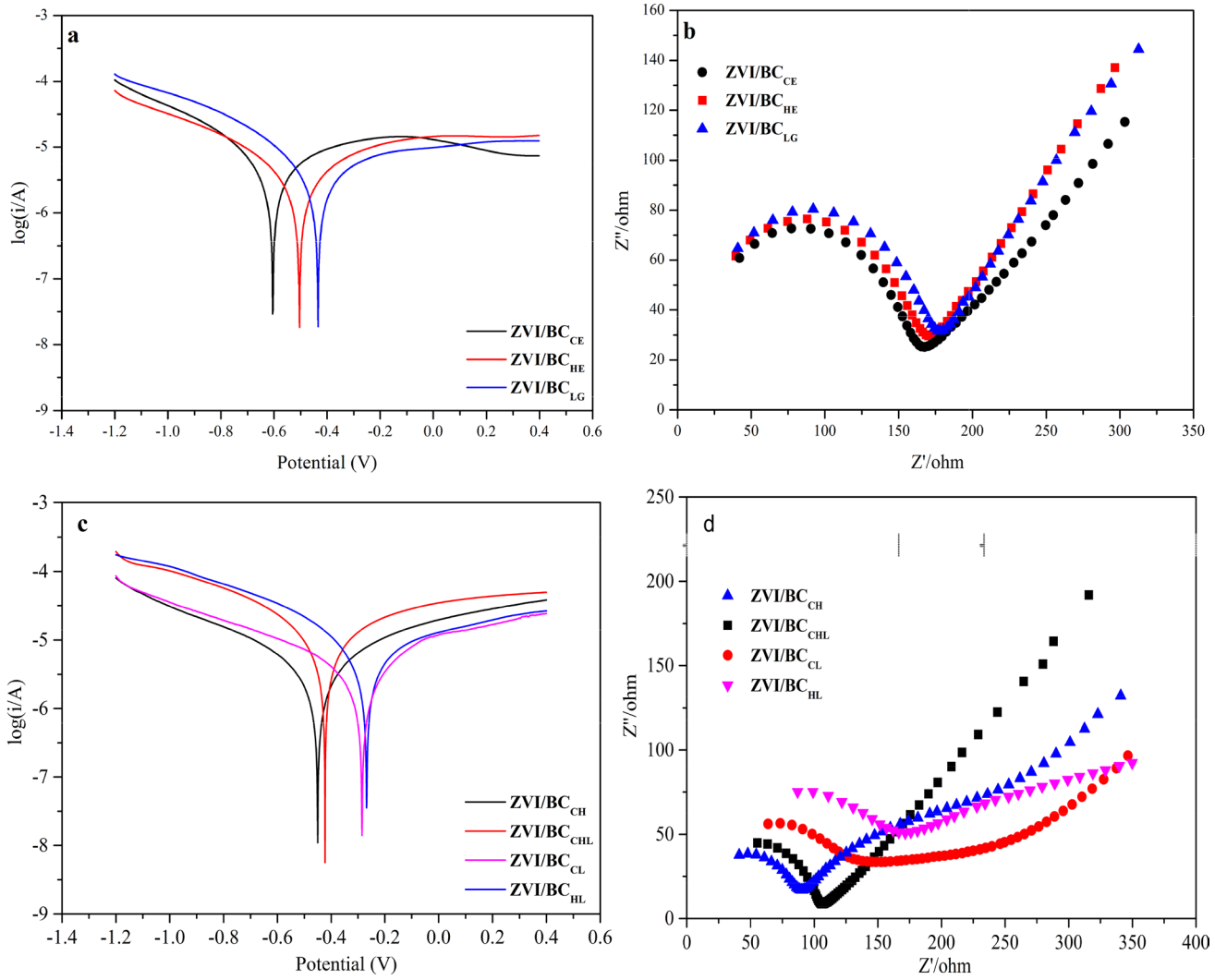

Fig. 8 Tafel corrosion curves (**a** and **c**) of ZVI/BC from single component (ZVI/BC_{CE}, ZVI/BC_{HE}, and ZVI/BC_{LG}) and mixed components (ZVI/BC_{CH}, ZVI/BC_{CL}, ZVI/BC_{HL}, and ZVI/BC_{CHL}) in 50 mg L^{-1} Cr(VI) solution. Nyquist plots (**b** and **d**) of ZVI/BC from single components and mixed components in 5 mM $K_3Fe(CN)_6$ and 0.1 M KCl

Removal mechanism of Cr(VI)

The elimination capacities of Cr(VI) using the pristine biochar from three biomass model compounds (BC_{CE}, BC_{HE}, and BC_{LG}) were 6.67, 4.49, and 3.42 mg g^{-1}, respectively (Fig. 7a), which can be attributable to larger specific surface area and better electrical conductivity of BC_{CE} and BC_{HE} than that of BC_{LG} (Table 1 and Fig. S4). In this regard, biochar as both electron donor and electron shuttle can facilitate removal of Cr(VI), which has been demonstrated in a previous study (Xu et al. 2019); thus, better electrical conductivity of BC_{CE} and BC_{HE} can transfer the electron from the inside of biochar to Cr(VI). On the other hand, BC_{CE} and BC_{HE} have higher graphitization degree and stronger electrical conductivity than BC_{LG}, which can transfer the electrons from the electron donor moieties on the surface of biochar to Cr(VI). However, carbon matrix can be not the main reaction active site on ZVI/BC (Zhao et al. 2020). In our previous study, the removal capacity of the pure ZVI for Cr(VI) was 8.39 mg g^{-1} (Fig. 7a), which was significantly lower than that of ZVI/BC (36.12 mg g^{-1}) prepared at 1000 °C (Zhao et al. 2020). This indicated the strong synergetic effect of ZVI and BC, which is due to the enhanced electrical conductibility of high-temperature biochar, promoting the reduction of Cr(VI). In accordance with the XPS result (Fig. 9) of the spent ZVI/BCs, two Cr2p doublets were observed, which corresponded to the $Cr2p_{3/2}$ and $Cr2p_{1/2}$ orbitals (Zhou et al. 2020). The binding energy values of trivalent chromium are located at 576.9 and 586.8 eV, and those of hexavalent chromium are at 579.8 and 589.0 eV (Xu et al. 2019). The XPS analysis indicated that approximately 78.09–80.22% of Cr adsorbed on the surface of ZVI/BCs existed in the form of trivalent chromium and the rest 19.78–21.91% existed in the form of hexavalent chromium. Thus, chemical reduction was the main removal mechanism of Cr(VI) by ZVI/BCs.

In Fig. S5, the peaks at 723.8 eV and 725.6 eV corresponded to Fe $2p_{1/2}$ of divalent iron and trivalent iron, respectively; and the Fe 2p XPS peaks at 710.4 eV and 711.8 eV referred to as Fe $2p_{3/2}$ for divalent iron and trivalent iron, respectively (Du et al. 2016). After Cr(VI) treatment, ~ 8.33–9.47% of the ferrous species of ZVI/BCs were transformed to ferric species that was likely in the form of Fe_2O_3 (Zhang et al. 2021) (Fig. S5). This indicated that the ferrous species resulting from oxidation of zero-valent Fe can also reduce Cr(VI) to trivalent chromium. C1s peak could be deconvoluted into graphitic or aromatic C, phenolic and alcohol carbon, carbonyl carbon, and carboxyl peaks at binding energies of 284.9, 285.4, 286.4, and 288.1 eV, respectively (Lyu et al. 2017; Zhang et al. 2021). After reaction with Cr(VI) at pH 3.0, phenolic and carboxyl carbon were spent, resulting to enhanced intensities of carbonyl carbon (Fig. 10a, b, and c), which showed that Cr(VI) reduction can also be obtained by electron donating moieties of biochar, e.g., phenolic carbon and carboxyl carbon (Klüpfel et al. 2014). In terms of ZVI/BC_{LG} (Fig. 10c), after reacting with Cr(VI) the O=C-O apparently disappeared, indicating that the functional groups were involved in complexation with cationic Cr(III) and/or anionic Cr(VI). The protonated carboxyl with positive charge complexed with anionic Cr(VI) with negative charge, facilitating Cr(VI) elimination, which was in accordance with the high proportion of Cr(Vi) adsorption by ZVI/BC_{LG}.

Moreover, the XPS peaks of O1s can be deconvoluted into three sub-peaks at 531.2, 532.8, and 535.5 eV, which were referred to C-O/Fe–O, -OH, and C=O, respectively (Fig. 10d, e, and f) (Zhang et al. 2021; Zhou et al. 2021a, b, c). In comparison to pristine ZVI/BC, the -OH groups vanished and C-O/Fe–O proportion reduced in Cr-laden composites, which further demonstrated complexation could exist between functional groups and hexavalent chromium and/or Cr(III). The results agreed with previous studies in which carboxyl and hydroxyl functional groups in biochar are primarily responsible for sorption of potentially toxic elements (Zhou et al. 2016). Additionally, the Cr in Cr-laden composites could exist in the form of Cr–O covalent bond, such as Cr_2O_3, $Cr(OH)_3$, $Fe_xCr_{1-x}OH$, and $FeCr_2O_4$ (Sun et al. 2020). Furthermore, the generated ferrous and ferric oxides including FeOOH, Fe_3O_4, and Fe_2O_3 owing to the oxidation of ZVI

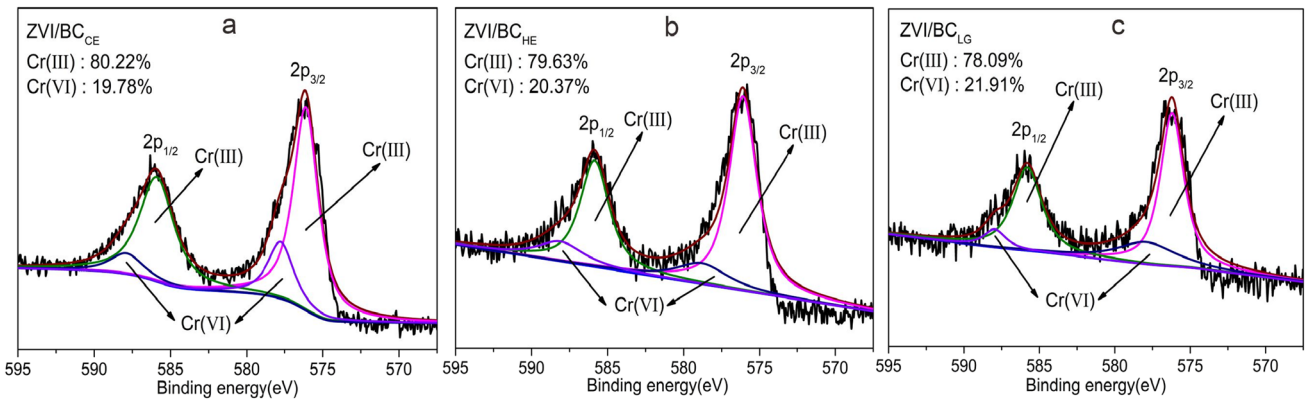

Fig. 9 X-ray photoelectron spectroscopy (XPS) spectrum of Cr2p after reaction with Cr(VI) for ZVI/BC_{CE} (**a**), ZVI/BC_{HE} (**b**), and ZVI/BC_{LG} (**c**)

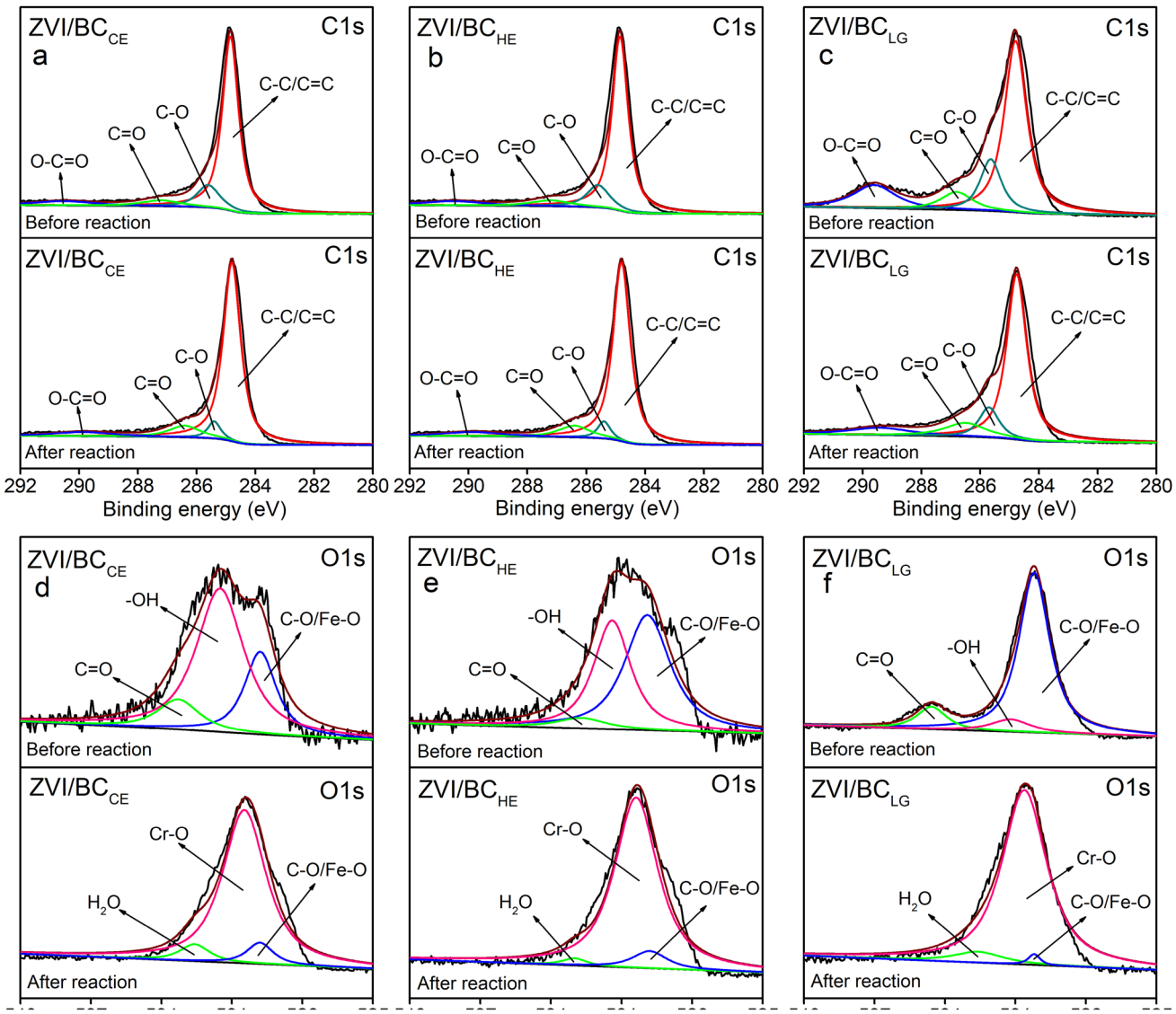

Fig. 10 X-ray photoelectron spectroscopy (XPS) spectrum of C1s and O1s before and after reaction with Cr(VI) for ZVI/BC_{CE} (**a** and **d**), ZVI/BC_{HE} (**b** and **e**), and ZVI/BC_{LG} (**c** and **f**)

can also contribute to the Cr(VI) adsorption via surface complexation (Dong et al. 2021). However, the removal capacity of the pristine BC_{CE}, BC_{HE}, and BC_{LG} were relatively low. Therefore, although the physical adsorption and the chemical complexation with functional groups existed, reduction predominated the removal mechanism of Cr(VI), which can be revealed by the XPS analysis and electrochemical analysis. Overall, the predominant reduction, following surface complexation, and co-precipitation were the mechanism for detoxification of Cr(VI) by ZVI/BC. In addition, the carbon matrix with more ordered and graphitic structure from cellulose and hemicellulose as an electron shuttle played an important role in facilitating the electron transfer from ZVI to hexavalent chromium. These findings were in agreement with the previous study (Zhou et al. 2021a, b, c). However, the carbon support from lignin component and its blends is not conducive to electron transfer of ZVI and removal of Cr(VI) because of the lower surface area and poor graphitization.

Conclusions

Hematite was co-pyrolyzed with three biomass modeling components (cellulose, hemicellulose, and lignin) and their blends to synthesize ZVI/BC. BCs and ZVI/BCs derived from cellulose and hemicellulose revealed greater carbon content and higher BET surface area than those from lignin. ZVI/B_{CE}, ZVI/BC_{HE}, and ZVI/BC_{CH} exhibited better graphitization owing to high-intensity carbonization

and decomposition of cellulose and hemicellulose. BCs from lignin and its hybrids compromised the removal capacity of ZVI/BC composites toward Cr(VI) owing to their amorphous structure and the poorer degree of graphitization. Lower Tafel corrosion potential and lower electron transfer resistance of ZVI/B_{CE}, ZVI/BC_{HE}, and ZVI/BC_{CH} indicated their higher electric conductivity and electron transfer rate, which facilitated electron transfer of ZVI to Cr(VI) and enhanced reduction and removal of Cr(VI) from solution. Chemical reduction, complexation, and co-precipitation played an important role in elimination of Cr(VI). This study provides an important evidence for screening biomass feedstock with higher contents of cellulose and hemicellulose to fabricate and optimize ZVI/BC composite with better Cr(VI) removal performance.

Supplementary Information The online version contains supplementary material available at https://doi.org/10.1007/s11356-021-17713-x.

Author contribution Jian Zhang: Conceptualization, data analysis, writing (original draft), software, methodology. Xianni Yang: Writing (original draft), software, and data analysis. Jun Shi: Software and data analysis. Mingyue Zhao: Conceptualization and data analysis. Weiqin Yin: Writing—reviewing and editing. Xiaozhi Wang: Writing—reviewing and editing. Shengsen Wang: Writing—reviewing and editing. Changai Zhang: Writing—reviewing and editing.

Funding This work was supported by the National Natural Science Foundation of China [41771349; 41977117; 41977085], Qing-Lan Project of Yangzhou University [2020], High-level Talent Support Plan of Yangzhou University [2019], Foreign Expert Recruitment Program of Jiangsu Province [BX2020050], Yangzhou Municipal Government-Yangzhou University joint research program [YZ2019137], Natural Science Research Project of Universities in Jiangsu Province of China [20KJB610014], and the Key Research and Development Program of Zhejiang Province [2019C02053].

Data availability All data generated or analyzed during this study are included in this published article and its supplementary information files.

Declarations

Ethical approval and consent to participate Not applicable.

Consent to Publish Not applicable.

Competing interests The authors declare no competing interests.

References

Chen RY (2017) Mechanism of iron oxide scale reduction in 5% H_2–N_2 gas at 650–900 °C. Oxid Met 88:687–717

Dhyani V, Bhaskar T (2018) A comprehensive review on the pyrolysis of lignocellulosic biomass. Renew Energ 129:695–716

Dong FX, Yan L, Zhou XH, Huang ST, Liang JY, Zhang WX, Guo ZW, Guo PR, Qian W, Kong LJ, Chu W, Diao ZH (2021) Simultaneous adsorption of Cr(VI) and phenol by biochar-based iron oxide composites in water: Performance, kinetics and mechanism. J Hazard Mater 416:125930

Dong H, Deng J, Xie Y, Zhang C, Jiang Z, Cheng Y, Hou K, Zeng G (2017) Stabilization of nanoscale zero-valent iron (nZVI) with modified biochar for Cr(VI) removal from aqueous solution. J Hazard Mater 332:79–86

Dong X, He L, Liu Y, Piao Y (2018) Preparation of highly conductive biochar nanoparticles for rapid and sensitive detection of 17β-estradiol in water. Electrochim Acta 292:55–62

Du J, Bao J, Lu C, Werner D (2016) Reductive sequestration of chromate by hierarchical FeS@Fe^0 particles. Water Res 102:73–81

Fan J, Chen X, Xu Z, Xu X, Zhao L, Qiu H, Cao X (2020) One-pot synthesis of nZVI-embedded biochar for remediation of two mining arsenic-contaminated soils: arsenic immobilization associated with iron transformation. J Hazard Mater 398:122901

Gabhi R, Basile L, Kirk DW, Giorcelli M, Tagliaferro A, Jia CQ (2020) Electrical conductivity of wood biochar monoliths and its dependence on pyrolysis temperature. Biochar 2:369–378

Gindl-Altmutter W, Köhnke J, Unterweger C, Gierlinger N, Keckes J, Zalesak J, Rojas OJ (2019) Lignin-based multiwall carbon nanotubes. Compos Part A Appl Sci Manufacturing 121:175–179

Giudicianni P, Cardone G, Ragucci R (2013) Cellulose, hemicellulose and lignin slow steam pyrolysis: Thermal decomposition of biomass components mixtures. J Anal Appl Pyrol 100:213–222

Guo S, Yang W, You L, Li J, Chen J, Zhou K (2020) Simultaneous reduction of Cr(VI) and degradation of tetracycline hydrochloride by a novel iron-modified rectorite composite through heterogeneous photo-Fenton processes. Chem Eng J 393:124758

Hoekstra J, Beale AM, Soulimani F, Versluijs-Helder M, van de Kleut D, Koelewijn JM, Geus JW, Jenneskens LW (2016) The effect of iron catalyzed graphitization on the textural properties of carbonized cellulose: magnetically separable graphitic carbon bodies for catalysis and remediation. Carbon 107:248–260

Jiang F, Yao Y, Natarajan B, Yang C, Gao T, Xie H, Wang Y, Xu L, Chen Y, Gilman J, Cui L, Hu L (2019a) Ultrahigh-temperature conversion of biomass to highly conductive graphitic carbon. Carbon 144:241–248

Jiang S, Ling L, Chen W, Liu W, Li D, Jiang H (2019b) High efficient removal of bisphenol A in a peroxymonosulfate/iron functionalized biochar system: mechanistic elucidation and quantification of the contributors. Chem Eng J 359:572–583

Johra FT, Lee JW, Jung WG (2014) Facile and safe graphene preparation on solution based platform. J Ind Eng Chem 20:2883–2887

Klüpfel L, Keiluweit M, Kleber M, Sander M (2014) Redox properties of plant biomass-derived black carbon (biochar). Environ Sci Technol 48:5601–5611

Li D, Zhong Y, Wang H, Huang W, Peng P (2021) Remarkable promotion in particle dispersion and electron transfer capacity of sulfidated nano zerovalent iron by coating alginate polymer. Sci Total Environ 759:143481

Lin H, Liu Y, Chang Z, Yan S, Liu S, Han S (2020) A new method of synthesizing hemicellulose-derived porous activated carbon for high-performance supercapacitors. Micropor Mesopor Mater 292:109707

Liu Y, Wang J (2019) Reduction of nitrate by zero valent iron (ZVI)-based materials: a review. Sci Total Environ 671:388–403

Lyu H, Tang J, Huang Y, Gai L, Zeng EY, Liber K, Gong Y (2017) Removal of hexavalent chromium from aqueous solutions by a novel biochar supported nanoscale iron sulfide composite. Chem Eng J 322:516–524

Ma Z, Wang J, Zhou H, Zhang Y, Yang Y, Liu X, Ye J, Chen D, Wang S (2018) Relationship of thermal degradation behavior and chemical structure of lignin isolated from palm kernel shell under different process severities. Fuel Process Technol 181:142–156

Ma Z, Yang Y, Wu Y, Xu J, Peng H, Liu X, Zhang W, Wang S (2019) In-depth comparison of the physicochemical characteristics of bio-char derived from biomass pseudo components: Hemicellulose, cellulose, and lignin. J Anal Appl Pyrol 140:195–204

Mian MM, Liu G (2019) Sewage sludge-derived TiO_2/Fe/Fe_3C-biochar composite as an efficient heterogeneous catalyst for degradation of methylene blue. Chemosphere 215:101–114

Monazam ER, Breault RW, Siriwardane R (2014) Reduction of hematite (Fe_2O_3) to wüstite (FeO) by carbon monoxide (CO) for chemical looping combustion. Chem Eng J 242:204–210

Mortazavian S, An H, Chun D, Moon J (2018) Activated carbon impregnated by zero-valent iron nanoparticles (AC/nZVI) optimized for simultaneous adsorption and reduction of aqueous hexavalent chromium: Material characterizations and kinetic studies. Chem Eng J 353:781–795

Neeli ST, Ramsurn H (2018) Synthesis and formation mechanism of iron nanoparticles in graphitized carbon matrices using biochar from biomass model compounds as a support. Carbon 134:480–490

Qian L, Zhang W, Yan J, Han L, Chen Y, Ouyang D, Chen M (2017) Nanoscale zero-valent iron supported by biochars produced at different temperatures: synthesis mechanism and effect on Cr(VI) removal. Environ Pollut 223:153–160

Ruan Y, Zhang H, Yu Z, Diao Z, Song G, Su M, Hou L, Chen D, Wang S, Kong L (2022) Phosphate enhanced uranium stable immobilization on biochar supported nano zero valent iron. J Hazard Mater 424:127119

Shi J, Wang J, Wang W, Teng W, Zhang W (2019) Stabilization of nanoscale zero-valent iron in water with mesoporous carbon (nZVI@MC). J Environ Sci 81:28–33

Sun T, Levin BDA, Guzman JJL, Enders A, Muller DA, Angenent LT, Lehmann J (2017) Rapid electron transfer by the carbon matrix in natural pyrogenic carbon. Nat Commun 8:14873

Sun T, Levin BDA, Schmidt MP, Guzman JJL, Lehmann J (2018) Simultaneous quantification of electron transfer by carbon matrices and functional groups in pyrogenic carbon. Environ Sci Technol 52:8538–8547

Sun X, Fang JM, Xu R, Wang M, Yang H, Han Z, Xu J (2020) Nanoscale zero-valent iron immobilized inside the mesopores of ordered mesoporous carbon by the "two solvents" reduction technique for Cr(VI) and As(V) removal from aqueous solution. J Mol Liq 315:113598

Wang L, Mu G, Tian C, Sun L, Zhou W, Yu P, Yin J, Fu H (2013) Porous graphitic carbon nanosheets derived from cornstalk biomass for advanced supercapacitors. Chemsuschem 6:880–889

Wang S, Zhao M, Zhou M, Li YC, Wang J, Gao B, Sato S, Feng K, Yin W, Igalavithana AD, Oleszczuk P, Wang X, Ok YS (2019a) Biochar-supported nZVI (nZVI/BC) for contaminant removal from soil and water: A critical review. J Hazard Mater 373:820–834

Wang S, Zhao M, Zhou M, Zhao Y, Li YC, Gao B, Feng K, Yin W, Ok YS, Wang X (2019b) Biomass facilitated phase transformation of natural hematite at high temperatures and sorption of Cd^{2+} and Cu^{2+}. Environ Int 124:473–481

Wang Y, Liu S, Huang P, Xie H, Qiao X (2019c) Structural and magnetic properties of mono-dispersed iron carbide (Fe_xC_y) nanoparticles synthesized by facile gas phase reaction. Ceram Int 45:11119–11124

Wu S, Shen D, Hu J, Zhang H, Xiao R (2016) Cellulose-hemicellulose interactions during fast pyrolysis with different temperatures and mixing methods. Biomass Bioenerg 95:55–63

Wu Y, Wu S, Zhang H, Xiao R (2018) Cellulose-lignin interactions during catalytic pyrolysis with different zeolite catalysts. Fuel Process Technol 179:436–442

Xu L, Zhang W, Yang Q, Ding Y, Yu W, Qian Y (2005) A novel route to hollow and solid carbon spheres. Carbon 43:1090–1092

Xu X, Huang H, Zhang Y, Xu Z, Cao X (2019) Biochar as both electron donor and electron shuttle for the reduction transformation of Cr(VI) during its sorption. Environ Pollut 244:423–430

Ye S, Yan M, Tan X, Liang J, Zeng G, Wu H, Song B, Zhou C, Yang Y, Wang H (2019) Facile assembled biochar-based nanocomposite with improved graphitization for efficient photocatalytic activity driven by visible light. Appl Catal B Environ 250:78–88

Yu J, Paterson N, Blamey J, Millan M (2017) Cellulose, xylan and lignin interactions during pyrolysis of lignocellulosic biomass. Fuel 191:140–149

Yu J, Tang L, Pang Y, Zeng G, Feng H, Zou J, Wang J, Feng C, Zhu X, Ouyang X, Tan J (2020) Hierarchical porous biochar from shrimp shell for persulfate activation: a two-electron transfer path and key impact factors. Appl Catal B Environ 260:118160

Zhang N, Eric M, Zhang C, Zhang J, Feng K, Li Y, Wang S (2021) ZVI impregnation altered arsenic sorption by ordered mesoporous carbon in presence of Cr(VI): a mechanistic investigation. J Hazard Mater 414:125507

Zhang W, Li R, Zhao X, Chen Z, Law AWK, Zhou K (2018a) A cobalt-based metal–organic framework as cocatalyst on $BiVO_4$ photoanode for enhanced photoelectrochemical water oxidation. Chemsuschem 11:2710–2716

Zhang X, Zhang K, Li H, Wang Q, Jin L, Cao Q (2018b) Synthesis of porous graphitic carbon from biomass by one-step method And its role in the electrode for supercapacitor. J Appl Electrochem 48:415–426

Zhao M, Zhang C, Yang X, Liu L, Wang X, Yin W, Li YC, Wang S, Fu W (2020) Preparation of highly-conductive pyrogenic carbon-supported zero-valent iron for enhanced Cr(VI) reduction. J Hazard Mater 396:122712

Zhou C, Han C, Min X, Yang T (2021a) Enhancing arsenic removal from acidic wastewater using zeolite-supported sulfide nanoscale zero-valent iron: the role of sulfur and copper. J Chem Technol Biotechnol 96:2042–2052

Zhou C, Han C, Min X, Yang T (2021) Simultaneous adsorption of As(V) and Cr(VI) by zeolite supporting sulfide nanoscale zero-valent iron: competitive reaction, affinity and removal mechanism. J Mol Liq 338:116619

Zhou C, Han C, Min X, Yang T (2022) Effect of different sulfur precursors on efficient chromium(VI) removal by ZSM-5 zeolite supporting sulfide nano zero-valent iron. Chem Eng J 427:131515

Zhou L, Liu Y, Liu S, Yin Y, Zeng G, Tan X, Hu X, Hu X, Jiang L, Ding Y, Liu S, Huang X (2016) Investigation of the adsorption-reduction mechanisms of hexavalent chromium by ramie biochars of different pyrolytic temperatures. Bioresource Technol 218:351–359

Zhou M, Yang X, Sun R, Wang X, Yin W, Wang S, Wang J (2021) The contribution of lignocellulosic constituents to Cr(VI) reduction capacity of biochar-supported zerovalent iron. Chemosphere 263:127871

Zhou M, Zhang C, Yuan Y, Mao X, Li Y, Wang N, Wang S, Wang X (2020) Pinewood outperformed bamboo as feedstock to prepare biochar-supported zero-valent iron for Cr^{6+} reduction. Environ Res 187:109695

Zhu Y, Li H, Zhang G, Meng F, Li L, Wu S (2018) Removal of hexavalent chromium from aqueous solution by different surface-modified biochars: acid washing, nanoscale zero-valent iron and ferric iron loading. Bioresource Technol 261:142–150